International Journal of Applied Earth Observation and Geoinformation 12 (2010) 496–505

Contents lists available at ScienceDirect

International Journal of Applied Earth Observation and Geoinformation

journal homepage: www.elsevier.com/locate/jag

Surface deformation associated with the 2008 Ms8.0 Wenchuan earthquake from ALOS L-band SAR interferometry

Guoxiang Liu[a,*], Jonathan Li[b], Zhu Xu[a], Jicang Wu[c], Qiang Chen[a], Huixin Zhang[a], Rui Zhang[a], Hongguo Jia[a], Xiaojun Luo[a]

[a] Department of Surveying Engineering, Southwest Jiaotong University, Chengdu, Sichuan, China
[b] Department of Geography and Environmental Management, University of Waterloo, Canada
[c] Department of Surveying and Geo-Informatics, Tongji University, Shanghai, China

ARTICLE INFO

Article history:
Received 22 July 2009
Accepted 20 May 2010

Keywords:
ALOS
L-band InSAR
GPS
Wenchuan earthquake
Deformation mapping

ABSTRACT

The Ms8.0 Wenchuan earthquake (in China) occurred on 12 May 2008 as a result of slip on the northeastern-striking Longmen Shan (LMS) faults beneath the rugged margin between the Qinghai-Tibet Plateau and Sichuan Basin. The catastrophic event caused significant surface ruptures and permanent ground displacement in a wide area. This paper concentrates on mapping surface deformation caused by the main shock with the interferometric synthetic aperture radar (InSAR) technology. The coseismic interferogram covering an area of over 83,000 km^2 is computed with use of 46 SAR images that were collected along 6 adjacent ascending orbits by the L-band SAR sensor onboard the Japanese Advanced Land Observing Satellite (ALOS). The displacements measured at 16 GPS sites are used to check the accuracy of the InSAR deformation measurements. The radar coherence is computed and analyzed in relation to the topography and the normalized difference vegetation index (NDVI) estimated from the Landsat-7 imagery. The results show that the coseismic surface deformation can be mapped up to a centimeter-accuracy level even over the highly mountainous and heavily vegetated area with the L-band interferometer. It is also demonstrated that the L-band interferograms with time interval of months to years can still maintain acceptable radar coherence for deformation extraction over the area under the extreme conditions. The extracted InSAR deformation measurements show that the lands in the Sichuan Basin had moved 0.1–1.3 m toward the satellite along the radar line of sight (LOS) direction with an azimuth of 349.8° and an elevation angle of 51.3°, while the lands in the LMS area had moved 1.4 m at most away from the satellite.

© 2010 Elsevier B.V. All rights reserved.

1. Introduction

The Ms8.0 Wenchuan earthquake occurred on 12 May 2008 in Sichuan Province, China. The seismic fracture took place on the northeastern-striking Longmen Shan (LMS) faults beneath the rugged eastern margin of the Qinghai-Tibet Plateau, resulting in complicated and large-scale surface ruptures and permanent displacement in a wide area (Wang et al., 2008; Yarai et al., 2008; Zhang, 2008; Huang and Li, 2009). This earthquake had the largest impact of any earthquake to strike China since the catastrophic 1976 Tangshan earthquake. According to the official report, the quake caused near 70,000 known deaths; more than 17,000 people are listed as missing, and over 370,000 injured (Hao et al., 2009).

The quantitative analysis of the coseismic surface deformation due to the major earthquake play a vital role in understanding the earthquake mechanisms in this region with complex tectonic settings (Burchfiel et al., 1995). Existing studies have presented the GPS-based deformation measurements around the rupture zone (Wang et al., 2008; Zhang, 2008). However, the short-wavelength deformation signature cannot be detected with the sparse GPS data that has very low spatial resolution (Liu et al., 2004; Liu, 2006; Zhang et al., 2008). It is very difficult and time consuming to collect the detailed deformation data along the entire fault system with any ground-based survey campaign. The limiting factors for fieldwork along the LMS faults include the inaccessibility of the highly mountainous areas, the risk of land-sliding, and the road blockage in the remote deep valleys.

Satellite interferometric synthetic aperture radar (InSAR) has been proven viable and efficient for mapping surface deformation related to, e.g., volcanic, earthquake, and urban subsiding activities (e.g., Massonnet et al., 1993; Massonnet and Feigl, 1998; Rosen et al., 2000; Pritchard and Simons, 2002; Ding et al., 2004; Zhang et al., 2008; Liu et al., 2009). For better understanding of coseismic surface movements, the area-based deformation measurements by InSAR

* Corresponding author. Tel.: +86 28 87601656; fax: +86 28 87600612.
E-mail addresses: rsgxliu@gmail.com, rsgxliu@swjtu.edu.cn (G.X. Liu).

0303-2434/$ – see front matter © 2010 Elsevier B.V. All rights reserved.
doi:10.1016/j.jag.2010.05.005

can greatly complement the point-based measurements by other geodetic technique such as GPS. However, the temporal decorrelation between SAR acquisitions often makes InSAR less robust (Zebker and Villasenor, 1992), particularly over the rugged and vegetated areas.

Existing studies (Zebker and Villasenor, 1992; Rosen et al., 2000; Li et al., 2008) indicated that the long-wavelength SAR sensor (e.g., L-band for JERS-1) is more robust than the short-wavelength one (e.g., C-band for ERS-1/2, Radarsat-1/2, and ENVISAT) in terms of temporal correlation for the success of interferometric analysis over vegetated areas. As a new generation of L-band SAR system, the Phased Array type L-band SAR (PALSAR) onboard the Japanese Advanced Land Observing Satellite (ALOS), which is a follow-on Japanese mission to JERS-1 and was launched on 24 January 2006, has recently demonstrated its unique advantage in detecting crustal deformation associated with some seismic events (e.g., Fukushima et al., 2008; Takada et al., 2009).

As the area stricken by the Wenchuan earthquake is highly mountainous and heavily vegetated, one tends to use the multiple PALSAR images to measure the coseismic surface deformation around the LMS fault zone. Several research groups have recently reported some deformation results due to the main shock with the ALOS interferometry (Ge et al., 2008; Sun et al., 2008; Shan et al., 2009). However the quality assessment of the coseismic deformation measurements associated with the Wenchuan earthquake has not been performed. Moreover, the applicability of the ALOS L-band interferometer has been rarely addressed for the area under the extreme conditions as the SAR system was newly launched.

This study concentrates on mapping surface deformation caused by the main shock with the 46 PALSAR images collected before and after the earthquake. The displacements measured at 16 GPS sites will be used to validate the accuracy of deformation measurements derived interferometrically. To demonstrate the capacity of the PALSAR sensor, the radar coherence will be analyzed in relation to the topography and the normalized difference vegetation index (NDVI) estimated from Landsat-7 multi-spectral images.

2. Tectonic setting and Ms8.0 Wenchuan earthquake

The 2008 Ms8.0 Wenchuan earthquake occurred on the northeastern-striking thrust Longmen Shan (LMS) faults beneath the rugged margin between the Qinghai-Tibet Plateau and Sichuan Basin (Fig. 1). The epicenter with a depth of about 19 km was located at 31.02°N and 103.37°E (Zhang, 2008; Shan et al., 2009), and close to the Town of Yingxiu in Wenchuan County that is 80 km west-northwest of Chengdu, the capital of Sichuan Province. Over 1000 aftershocks, some exceeding magnitude 6, continued to strike the area even months after the main shock (Wikipedia, 2009).

As shown in Fig. 1, the LMS fault zone consists of three major branches, the Guanxian–Anxian (GX–AX), Yingxiu–Beichuan (YX–BC), and Wenchuan–Maoxian (WC–MX) faults (Burchfiel et al., 1995; Hao et al., 2009). These faults are generated due to the collision between the Indo-Australian Plate and the Eurasian Plate (Burchfiel et al., 1995; Densmore et al., 2007). Such tectonic setting caused large-scale structural deformation inside the Asian continent, resulting in a thickening crust of the Qinghai-Tibet Plateau, the uplift of its landscape and an eastward extrusion. Near the Sichuan Basin, the east-northward movement of the Qinghai-Tibet Plateau meets with strong resistance from the South China Block, causing a high degree of stress accumulation in the LMS thrust formation. This LMS region is roughly coincident with a Mesozoic collisional plate margin that developed during the closure of the Paleo-Tethys Ocean about 230–200 million years ago and continued into the Late Cretaceous (Burchfiel et al., 1995; Densmore et al., 2007).

As shown in Fig. 1, the area affected by the Wenchuan earthquake spans the transition zone between the Sichuan Basin and Qinghai-Tibet Plateau. The LMS region rises gradually westward from 500 to 4000 m above seal level, and some mountain peaks reach up to 6000 m. The terrain undulation is more than 5 km over distances of less than 50 km. The terrain slopes within the rugged area range between 20° and 60°. The plateau margin has the steepest topographic gradient of any edge of the present-day plateau (Densmore et al., 2007).

3. Dataset used for this study

To map the coseismic surface deformation over the area affected by the Wenchuan earthquake, we utilized a total of 46 SAR images acquired between 28 January 2007 and 22 June 2008 by the ALOS PALSAR along 6 ascending paths with number of 471 to 476. The flying direction of the satellite is 349.8° in azimuth. All the SAR images were collected at a nominal incidence angle of 38.7° in HH polarization. The coverage of SAR scenes of 6 paths is shown in Fig. 1. Some basic information of the radar acquisitions is listed in Table 1.

For each path, we concatenated and processed all the along-path raw radar images (at Level 0) in several consecutive frames, thus yielding a single look complex (SLC) image with a pixel spacing of 4.7 m in slant range and 3.2 m in azimuth. Both the range and azimuth timing information in the parameter files corresponding to the raw radar images were used to determine the overlaps and confirm the along-path consistency. A simple overlay operation was applied to mosaick over the matched overlaps. The merged SLC images acquired along each path before and after the main shock were combined to form an interferometric pair for deformation extraction. The key parameters of 6 interferometric pairs corresponding to the path 471–476 are summarized in Table 1. The maximum time interval and perpendicular baseline are 506 days and 464.2 m, respectively.

To facilitate the ALOS InSAR processing, a digital elevation model (DEM) derived from the Shuttle Radar Topography Mission (SRTM) with 3 arcsec resolution was used to remove the topographic components from interferograms. The DEM data of the study area is depicted as a shaded relief map in Fig. 1. The three-dimensional (3D) coseismic surface displacements derived by GPS at the 16 sites (see Fig. 1) by Zhang (2008) were used to validate the interferometric results. In support of quantitative analysis of interferometric coherence, several multi-spectral images taken by the enhanced thematic mapper (ETM) onboard satellite Landsat-7 were used to compute the normalized difference vegetation index (NDVI) over the study area.

It should be noted that the study area corresponds to mountains with dense vegetation or plain parts with fertile farmlands and residential centers. As the Sichuan Basin possesses the highly variable climate, the study area is often covered by clouds and rainfalls occur frequently.

4. Methods for data reduction

In order to extract the coseismic surface deformation due to the Wenchuan earthquake, we performed data reduction with all interferometric pairs as listed in Table 1. The methods and procedures of interferometric analysis are briefly described in this section.

4.1. Generation of raw interferogram and coherence map

The extraction of coseismic deformation from each interferometric pair started from generating a raw interferogram by a conjugate multiplication of the two co-registered SLC images

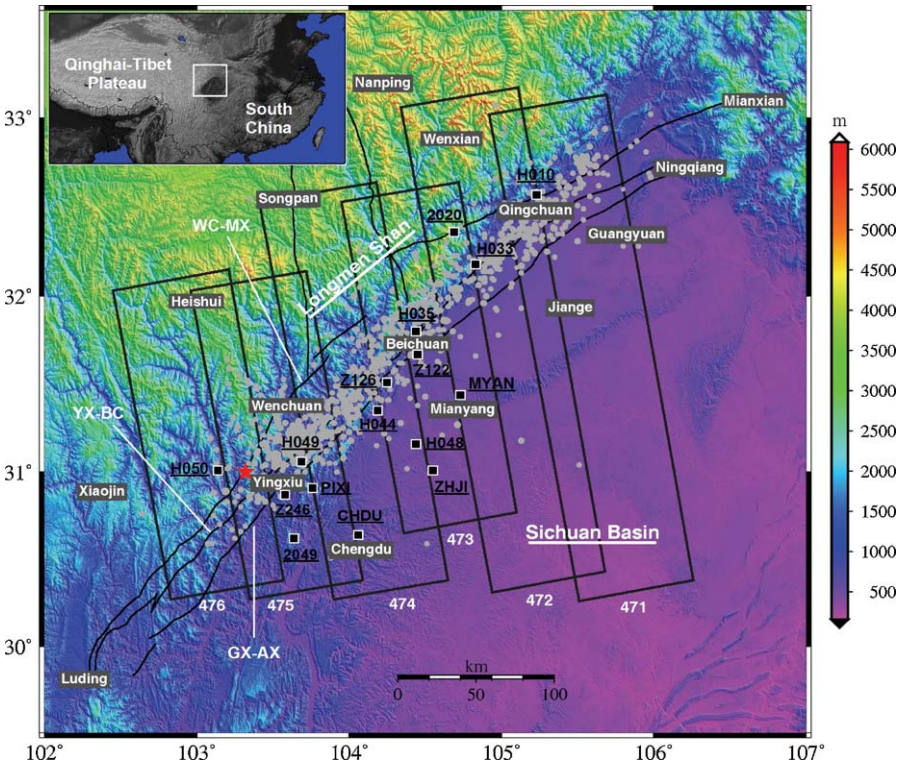

Fig. 1. Location map of LMS and Sichuan Basin with some placenames annotated. The epicenter of Wenchuan earthquake is marked by a red star, and the aftershocks are shown by gray dots. Overlaid onto the terrain relief are the LMS faults and the PALSAR scenes used for mapping the coseismic deformation. The 16 GPS sites are indicated by black squares. The topography is taken from the SRTM DEM, while the faults are simplified from the work by Zhang (2008). (For interpretation of the references to color in the figure caption, the reader is referred to the web version of the article.)

acquired before and after the main shock, respectively, over the same area. Such operation can be expressed by (Liu, 2006)

$$IF(r,a) = M(r,a)\cdot S(r,a)^{*} \quad (r=1,2,\ldots,K;\ \ a=1,2,\ldots,L) \qquad (1)$$

where (r, a) denote image coordinates in slant range and azimuth, respectively; K and L are the image size in row and column, respectively; M and S are the complex values of the master and slave image, respectively; * denotes the complex conjugate operator; IF is the resultant complex value of the raw interferogram.

The argument of the complex value derived by Eq. (1) is interferometric phase (phase difference) φ between two epochs. The phase-difference pattern over the imaged area can be visualized by color fringes that contain several types of information (Massonnet and Feigl, 1998; Rosen et al., 2000):

(1) Flat-earth trend pattern that are of nearly parallel strips due to differences between two satellite trajectories.
(2) Topographic pattern that is a contour-shaped pattern depicting the terrain relief of the area.
(3) Change pattern that is caused by any range change in radar line of sight (LOS) direction between two epochs.

Possible sources of the resultant change pattern include the coseismic surface motion, range change due to atmospheric inhomogeneity in time and space, and random noise. The quality of interferogram can be measured by its corresponding coherence map. We calculated the coherence value $\hat{\gamma}$ for each pixel by a moving window with size of N (Ghiglia and Pritt, 1998; Rosen et al., 2000), i.e.,

$$\hat{\gamma} = \left| \frac{\left|\sum_{i=1}^{N} M_i \cdot S_i^{*}\right|}{\sqrt{\sum_{i=1}^{N}|M_i|^2 \cdot \sum_{i=1}^{N}|S_i|^2}} \right| \qquad (2)$$

where $\hat{\gamma} \in [0, 1]$. If $\hat{\gamma}$ reaches 0, it means that the radar signals between two epochs are totally decorrelated; if $\hat{\gamma}$ reaches 1, it means that the interferometric phase is least affected by noise.

There are two major factors responsible for coherence reduction (Zebker and Villasenor, 1992). First, the scattering properties of the imaged surface may alter between two epochs, thus resulting in temporal decorrelation. Second, the revisiting sensor observes the same resolution cell from different viewpoints, thus inducing a dissimilar interference pattern, i.e., spatial decorrelation. To enhance

Table 1
Parameters of 6 PALSAR interferometric pairs used in this study.

No.	Path no.	Frame no.	Date of acquisition	Strip center[a]		Time interval (days)	Perpendicular baseline (m)
				ζ (°)	η (°)		
1	471	600–640 (5 frames)	2008-2-29, 2008-5-31	105.604	31.701	92	208.4
2	472	600–640 (5 frames)	2007-1-28, 2008-6-17	105.030	31.720	506	156.0
3	473	610–630 (4 frames)	2008-2-17, 2008-5-19	104.530	31.680	92	359.8
4	474	600–630 (4 frames)	2008-3-5, 2008-6-5	104.045	31.454	92	464.2
5	475	600–620 (3 frames)	2007-6-20, 2008-6-22	103.541	31.208	368	283.6
6	476	600–620 (3 frames)	2008-4-8, 2008-5-24	103.027	31.209	46	183.2

[a] ζ and η stand for longitude and latitude, respectively.

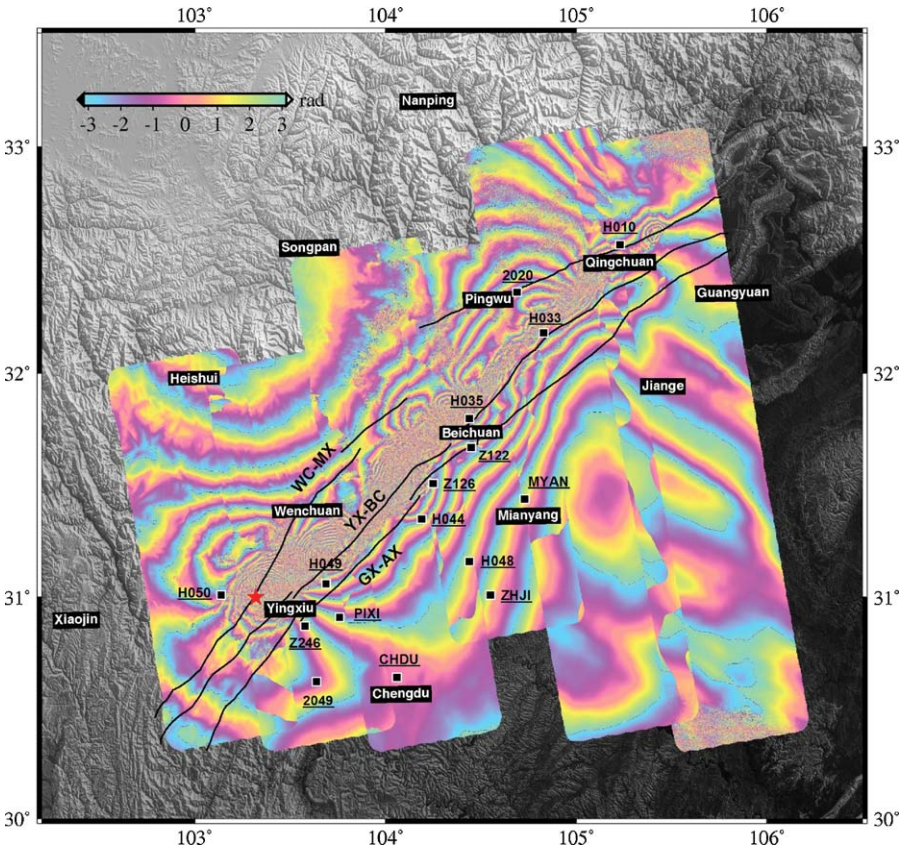

Fig. 2. The mosaicked coseismic interferogram reflecting surface displacements in radar LOS direction. The 16 GPS sites and the LMS faults are marked and some placenames are also annotated for better analysis.

signal-to-noise (SNR) ratio, we performed multilooking operation (6 looks in range and 14 looks in azimuth) to the raw interferogram, thus resulting in a resolution of 45 by 45 m.

4.2. Removal of flat-earth trend effects

In the case of a nonzero spatial baseline, the reference body (e.g., ellipsoidal surface) can result in range difference for each pixel between the two SAR passes (Liu, 2006). The equivalent phase differences that appear as nearly parallel strips are generally dominant in a raw interferogram, and need to be removed to highlight other information (Massonnet and Feigl, 1998). The range differences ΔR_{re} were first calculated for a set of tiepoints evenly distributed in the entire image with use of precise orbit data, and then modeled by a 3rd-order polynomial (Liu, 2006). Once the model is determined, the flat-earth trend effect *FT* of a pixel can be calculated by

$$FT(r,\ a) = \cos\left(\frac{4\pi}{\lambda}\Delta R_{ref}(r,a)\right) + i\cdot\sin\left(\frac{4\pi}{\lambda}\Delta R_{ref}(r,a)\right) \quad (3)$$

The flat-earth trend phases were removed from the raw interferogram by

$$IF_{flat}(r,a) = IF(r,a)\cdot FT(r,a)^* \quad (4)$$

where IF_{flat} denotes the resultant complex value of the flattened interferogram.

4.3. Removal of topographic effects

To highlight the coseismic surface movements, the topographic effects need to be removed from the flattened interferogram. Such procedure is referred to as differential interferometric processing (DIP). Currently, two DIP approaches are available, i.e., the two-pass method by Massonnet et al. (1993) and the three-pass method by Zebker et al. (1994). As the SRTM DEM is available for the study area, we preferred to employ the two-pass method for removal of topographic effects. The topographic phases φ_t were first simulated on a pixel-by-pixel basis with both the orbital data and the SRTM DEM (Rosen et al., 2000). The topographic effect *TE* of a pixel can be expressed by

$$TE(r,a) = \cos(\varphi_t(r,a)) + i\cdot\sin(\varphi_t(r,a)) \quad (5)$$

The topographic effects were then removed from the flattened interferogram by

$$IF_{dif}(r,a) = IF_{flat}(r,a)\cdot TE(r,a)^* \quad (6)$$

where IF_{dif} denotes the resultant complex value of the differential interferogram.

4.4. Ambiguity solution and deformation derivation

After derivation of all the along-path differential interferograms for 6 paths, we first transformed them in slant range projection into the Universal Transverse Mercator (UTM) coordinate system by a geocoding process with use of the same SRTM DEM (see Section 3). The interferograms derived in this way have the same posting and grid system. We then mosaicked them by a simple overlay operation over the overlapping areas between the across-path interferograms. The by-products such as amplitude and coherence images were also geocoded and mosaicked in the same way.

It should be emphasized that the differential phase value at each pixel is ambiguous to within the integer multiples of 2π, which should be determined by a phase unwrapping algorithm. We conducted phase unwrapping to the mosaicked differential interferogram by a path-following integration method (Ghiglia and Pritt,

Table 2
Comparison between GPS and InSAR displacements at 16 GPS sites.

No.	Site name	Coordinates		Displacements[a] (cm)			ΔR_{GPS} (cm)	ΔR_{In} (cm)	$d_{\Delta R}$ (cm)
		ζ (°)	η (°)	E–W	N–S	U–D			
1	H010	105.23	32.57	41.5	100.5	30	−12.3	−13.0	0.7
2	H033	104.83	32.18	−152.4	−14.3	−66.3	42.4	39.8	2.6
3	2020	104.69	32.36	68.6	25.1	−8.1	−50.4	−49.3	−1.1
4	MYAN	104.73	31.44	−30.5	6.6	−1.4	17.4	14.3	3.1
5	ZHJI	104.55	31.01	−20.3	7.3	−0.5	11.1	10.5	0.6
6	H044	104.19	31.35	−98.3	39.7	−12.3	47.7	45.5	2.2
7	CHDU	104.06	30.64	−15.8	11.7	−1.1	7.4	6.4	1.0
8	PIXI	103.76	30.91	−56.3	42.6	−8.1	24.4	22.2	2.2
9	2049	103.64	30.62	−11.8	12.0	−5.7	1.5	1.8	−0.3
10	Z246	103.58	30.87	−37.8	36.6	−15.6	7.0	5.5	1.5
11	H050	103.14	31.01	64.0	−37.4	−22.8	−53.4	−52.0	−1.4
12	H048	104.44	31.16	−30.3	9.9	−2.5	15.2	18.9	−3.7
13	Z126	104.25	31.51	−122.1	37.9	−20.4	57.5	50.5	7.0
14	H049	103.69	31.06	−127.6	80.1	−21.6	54.3	46.4	7.9
15	H035	104.44	31.8	−237.9	48.1	−67.5	87.4	100.2	−12.8
16	Z122	104.45	31.69	−94.5	43.9	−46.6	16.4	32.1	−15.7

[a] E–W, N–S and U–D stand for east–west, north–south and up–down motion component, respectively. The positives are eastward, northward and upward motions. The GPS data is taken from the work by Zhang (2008).

1998). As the phases unwrapping works on a very wide merged interferogram, this task significantly increases both memory cost and computation burden. We therefore divided the entire interferogram into the multiple blocks in row and column directions with an overlap of 150 pixels and performed phase unwrapping on a block-by-block basis. On the other hand, the abnormal phase jumps (larger than π radians) may propagate into the other parts, thus resulting in global errors in unwrapped phases. We therefore concentrated on manual editing of the connections of residues (i.e., branch cuts) by inspecting fault ruptures and coherence information, thus minimizing the error propagation in phase unwrapping.

Finally, the differential phase value ψ_m in absolute sense of a pixel can be converted to a range change ΔR_{In} in radar LOS direction due to the coseismic movement, i.e.,

$$\Delta R_{In} = \frac{\lambda}{4\pi} \cdot \psi_m \tag{7}$$

where λ is the radar wavelength (23.6 cm for ALOS PALSAR).

We summarize here the procedures described above. The raw interferogram and its coherence map were first generated on a path-to-path basis. Both the precise orbit data and the SRTM DEM were then used to successively remove the flat-earth trend and topographic effects from the raw interferogram, thus resulting in the differential interferogram of each path. All the differential (coseismic) interferograms of 6 paths were mosaicked and unwrapped. The unwrapped phases were finally converted to the LOS displacements, and the projection transform was applied to each of the interferometric products.

5. Results and discussion

5.1. Coseismic interferogram and its interpretation

Fig. 2 shows the mosaicked coseismic interferogram in UTM projection, which covers an area of more than 83,000 km^2. The 16 GPS sites and the LMS faults are marked in Fig. 2 and some placenames are also annotated for better analysis. Both the residual orbital errors and the possible atmospheric effects result in fringe discontinuities in some overlapping areas between the across-path interferograms. The entire fringes basically extend northeast and surround the LMS faults, whose pattern clearly reveals the surface ruptures and displacements due to the Wenchuan earthquake. Each fringe corresponds to a spatial variation of 11.8-cm surface displacements (half radar wavelength) in radar LOS direction. The 9–10 fringes can be identified in the Sichuan Basin, which are equivalent to the continuous LOS displacements of 100–120 cm. In the west side of the LMS faults, The 8–9 fringes are visible but appear more complicated in pattern, which correspond to the continuous LOS displacements of 90–110 cm. The fringe rates close to the faults are much higher than those far away from the faults. The fringe density in the Sichuan Basin is 2–3 times larger than that in the LMS areas.

As a number of aftershocks occurred between two epochs of each path, some surface motions caused by the aftershocks additionally contributed to the interferogram as shown in Fig. 2. For example, a small oval-shaped pattern can be seen in the upper part of path 471, which may be closely associated with the Ms6.4 aftershock occurring in Qingchuan on 25 May 2008 (Wikipedia, 2009). A lobe-shaped pattern in the upper part of path 472 may be highly associated with the Ms6.0 aftershock occurring in Jiangyou on 18 May 2008 (Wikipedia, 2009).

A closer inspection with Fig. 2 indicates that the fringes along the LMS faults, in particular the YX–BC and GX–AX faults, are very dense or become invisible due to loss of radar coherence. The remarkable coseismic surface ruptures in the fault zone caused serious temporal decorrelation between two SAR acquisitions so that the near-field displacements are not detectable in width of 6 km (toward Qingchuan) to 28 km (toward Yingxiu). Existing studies reported that both the YX–BC and GX–AX faults might rupture simultaneously according to their field investigation and fault-slip model inversion (Hao et al., 2009; Lin et al., 2009). Our results confirm that the surface ruptures of the main shock were primarily caused by the two active faults (YX–BC and GX–AX), extending about 280 km from southwest of the Town of Yinxiu to north of Qingchuan County.

Numerical analysis with the displacement map derived interferometrically shows that the lands in the Sichuan Basin had moved 0.1–1.3 m toward the satellite along the radar LOS direction with an azimuth of 349.8° and an elevation angle of 51.3°, while the lands in the LMS area had moved 1.4 m at most away from the satellite. The near-field displacements are significantly larger than the far-field ones. Such distribution of surface displacements can be well explained by convergent movements of the thrust LMS faults (Lin et al., 2009).

5.2. Accuracy of deformation measurements

The existing studies indicated that the accuracy of deformation measurements extracted from the coseismic interferogram is

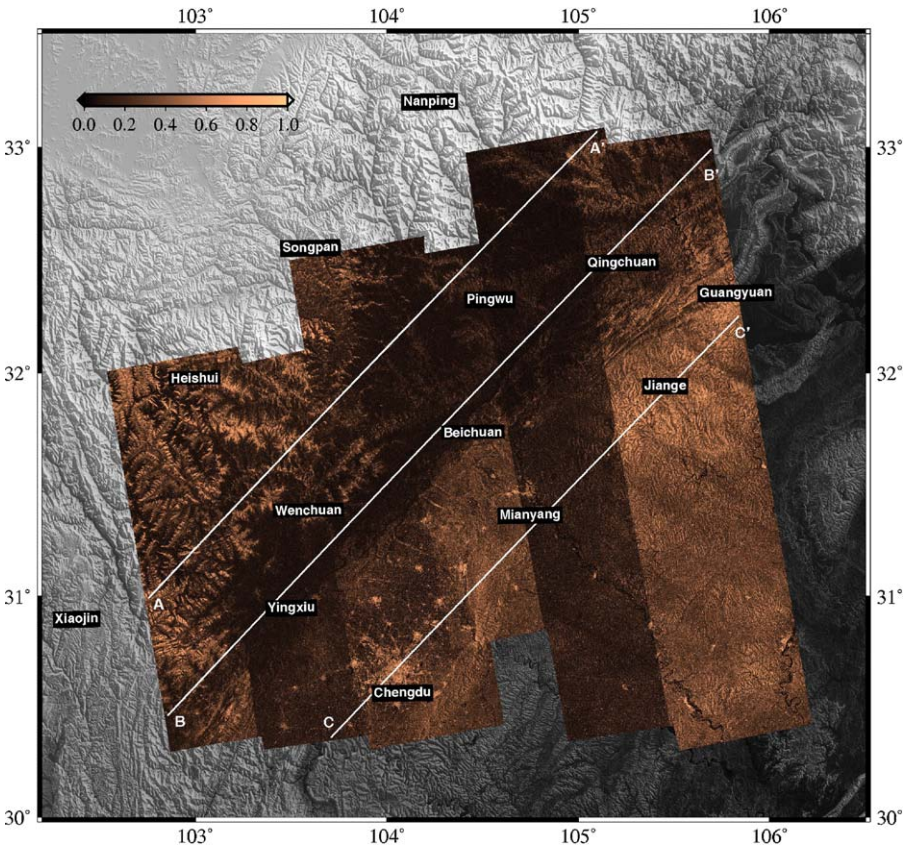

Fig. 3. The mosaicked coherence map indicating interferometric quality. Line AA′, BB′ and CC′ are marked for reference of Fig. 7.

affected by several major factors: (1) orbital errors, (2) DEM errors, (3) phase noises due to spatial and temporal decorrelation, and (4) atmospheric phase delays (Rosen et al., 2000; Liu et al., 2008; Ding et al., 2008). As the study area is dominated by mountains and variable humidity, the calibrations of orbital and atmospheric effects are actually the challenging tasks. We however applied a baseline refinement procedure (Liu, 2006) to correct the orbital errors during the interferogram computation.

As the SRTM DEM used in this study has an accuracy of 10 m in elevation, it can be estimated using Eq. (4) in Liu et al. (2004) that the displacement in radar LOS direction has an error of smaller than 10 mm for the interferometric pairs as listed in Table 1. The minimum and maximum errors in the LOS displacements due to the DEM errors are 3 and 8 mm for the pairs with the minimum and maximum perpendicular baselines of 156.0 and 464.2 m, respectively.

The random phase noises due to spatial and temporal decorrelation also cause uncertainties in deformation measurements. Given the fact that error in phase is 20°, we can infer with Eq. (7) that the accuracy of displacement is 6 mm for the ALOS L-band interferometer. In terms of spatial decorrelation, we estimated that the critical perpendicular baseline for the ALOS PALSAR interferometer is up to 17.5 km (see Zebker and Villasenor, 1992). As the perpendicular baselines of all interferograms used in this study are shorter than 500 m, the phase noise due to spatial decorrelation is negligible. We will address the temporal decorrelation in Section 5.3.

For the purpose of accuracy assessment, the independent 3D GPS data provided by Zhang (2008) were used to check the InSAR results. We first projected the 3D coseismic motion components derived by GPS at each of 16 sites onto radar LOS direction, and then compared them with the displacements derived by InSAR on a site-by-site basis. Table 2 lists the comparison between GPS (ΔR_{GPS}) and InSAR (ΔR_{In}) displacements in radar LOS direction at the GPS sites, where $d_{\Delta R}$ denotes the difference between ΔR_{GPS} and ΔR_{In}.

It can be seen from Table 2 that the 4 near-field sites, i.e., Z122, Z126, H035 and H049, have large discrepancies of 7–15 cm between the GPS and InSAR results. However, the two types of measurements at the remaining 12 sites are in good agreement, only differing in 1–3 cm. The differences $d_{\Delta R}$ at some sites may be overestimated due to deformations associated with the aftershocks. The statistical calculation with the 12 sites indicates that the mean and the standard deviation (SD) of differences are 0.62 and ±1.97 cm, respectively. This nevertheless demonstrates that the centimetre-level accuracy of deformation measurements can be achieved with the ALOS L-band SAR interferometer. The previous study showed that the ERS C-band SAR interferometer was able to measure the coseismic displacements up to 1-cm accuracy (e.g., Liu et al., 2004).

The large discrepancies at the near-field GPS sites may be attributed to the fact that GPS measures displacement at a single point while InSAR measures that over a resolution cell with a size of tens of square meters. As the near-field deformation gradients are extremely high, the multilooking and filtering operations must be applied to enhance phase SNR, thus resulting in a smoothened version of the detailed deformation features. Hence the InSAR measurements at the near-field GPS sites are in disagreement with the GPS results. In addition, we observed that phase unwrapping around the fault zones was really a challenging task, which might reduce the reliability in deformation measurements close to the faults.

5.3. Coherence analysis

As an indicator of interferometric quality, the mosaicked coherence map in UTM projection is shown in Fig. 3, where the line AA′, BB′ and CC′ are marked for later analysis. The black-yellowish color

bar represents a variation of coherence values from 0 to 1, meaning the lowest and highest SNR in phases. Since the spatial decorrelation is negligible as mentioned earlier, the coherence level of this study area is governed largely by temporal decorrelation (e.g., Zebker and Villasenor, 1992) and topographic effects (e.g., Lee and Liu, 2001; Liu, 2006).

A closer inspection with Fig. 3 and Table 1 indicates that the different time intervals between two SAR acquisitions for path 471–476 present the dissimilar levels of overall coherence. It should be emphasized again that the loss of coherence around the LMS faults is mainly due to the irregular coseismic surface ruptures as discussed earlier. The time intervals of over 1 year (506 days for path 472 and 368 days for path 475) caused a lower level of coherence, while the shorter time intervals of 1–3 months (46 days for path 476 and 92 days for path 471, 473 and 474) leaded to a higher level of coherence. However the urban areas can always keep long-term coherent radar backscattering due to the man-made objects, thus resulting in satisfactory coherence for different time intervals. For instances, the coherence values range between 0.45 and 0.65 over months to years in Chengdu (in path 474), Mianyang (in path 473) and Jiangyou (in path 472).

As far as the topographic factor is concerned, we observed from Fig. 3 that the coherence values in the farmlands of the flat Sichuan Basin are generally higher than those in the LMS areas with significant topography (20° to 60° slopes). To better analyze the relation between coherence and topography, we first grouped the terrain slopes (estimated for the study area with the SRTM DEM) into the 2°-range bins covering 0° to 60°, and then calculated the coherence mean and SD for each of slope bins. As shown in Fig. 4, the interferometric coherence is represented as a function of terrain slopes, where the coherence mean and SD are indicated by square and error bar, respectively. It is clear that the coherence values generally drop with increase of slopes that cause geometric distortion to the SAR images. The coherence values decrease almost linearly from 0.5 to 0.3 between the slopes of 0° and 20°. When the slopes are greater than 20°, the coherence values vary around 0.3 with insignificant drop rate. However, the abnormal cases can be seen at the smallest and greatest slopes. This can be explained by that the size of coherence samples in the two bins is small and may cause under- or over-estimation of the statistical parameters.

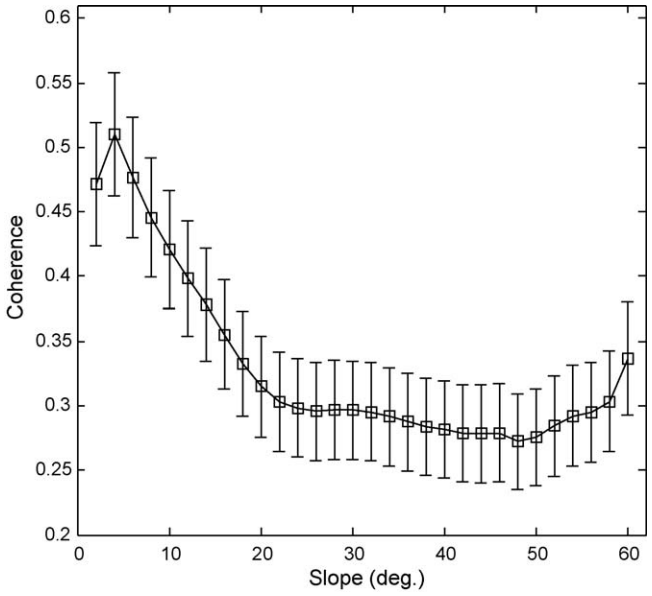

Fig. 4. The interferometric coherence is represented as a function of terrain slopes. The coherence mean and SD for each of the slope bins are indicated by square and error bar, respectively.

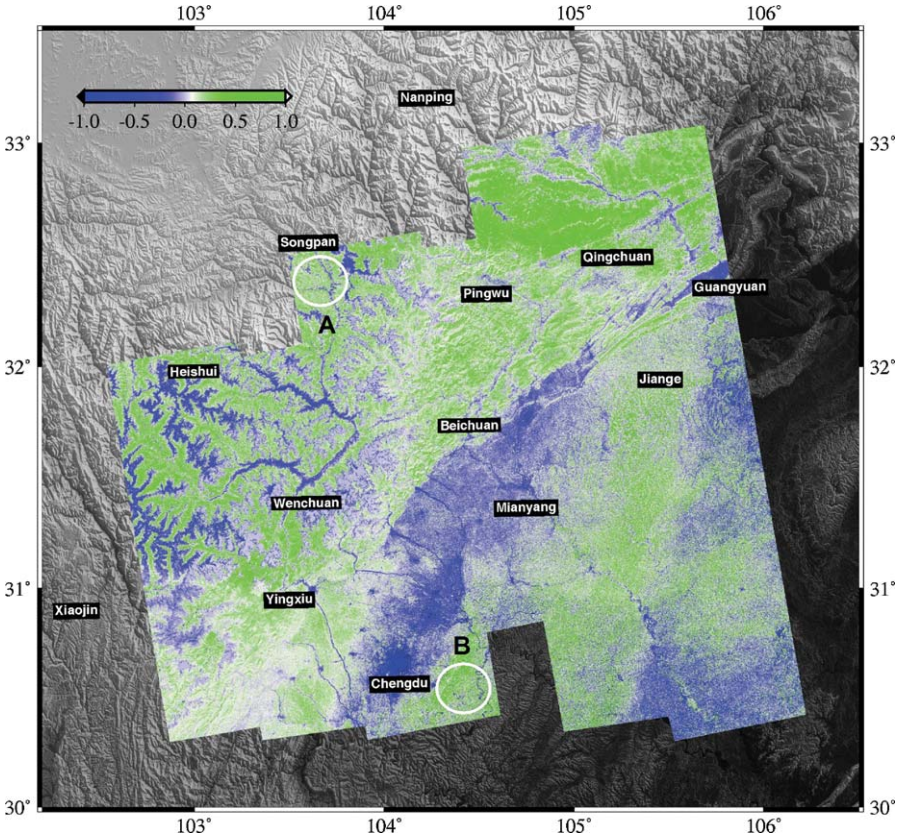

Fig. 5. The NDVI map of the study area. The original Landsat-7 data is courtesy of USGS. The two ellipses, A and B, are marked for better analysis.

The previous studies found that the vegetation factor is a major source for temporal decorrelation (e.g., Zebker and Villasenor, 1992; Rosen et al., 2000; Liu, 2006). We extracted vegetation data to help understand how the radar coherence is affected by plant canopies. As done by Vancutsem et al. (2009), a NDVI map in the coverage of all the PALSAR scenes was computed by using the red and near-infrared band data of several Landsat-7 ETM multi-spectral images which are freely available from the U.S. Geological Survey (USGS). Fig. 5 displays the so-obtained NDVI map where the green stands for the densest canopies (NDVI = 1), and the blue for the non-vegetated parts (NDVI = −1).

The NDVI map exhibits that over 70% of the entire study area is covered by a combination of bushes, coniferous and broad-leaved trees. A detailed comparison between Figs. 3 and 5 shows that the coherence values in the areas with higher NDVI are generally smaller than those in the areas with lower NDVI. This can be explained the plant canopies that often alter with time due to their natural growth, leaf fluttering due to wind effects and change of water content in leaves. Such temporal changes cause the incoherent radar backscattering between two SAR acquisitions. Nevertheless it should be pointed out that the L-band SAR interferometer can map the coseismic deformation with interferograms over months to years due to its capability of penetrating into canopies more deeply.

For the quantitative correlation analysis between coherence and NDVI, we first grouped the NDVI values in the study area into the 0.1-range bins covering −1 through 1, and then calculated the coherence mean and SD for each of NDVI bins. As shown in Fig. 6, the interferometric coherence in statistical sense is represented as a function of NDVI values. The coherence values generally drop from 0.5 to 0.25 with increase of NDVI values, meaning that the higher the vegetation density, the lower the interferometric coherence. However, the abnormal cases can be seen around the NDVI values of 0.5 and 0.6–1. These are most likely affected by the types of canopies.

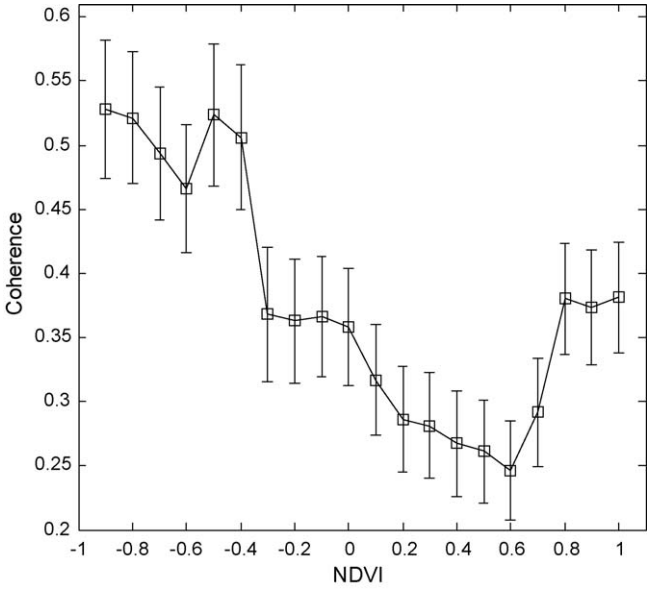

Fig. 6. The interferometric coherence is represented as a function of NDVI. The coherence mean and SD for each of the slope bins are indicated by square and error bar, respectively.

From the above analysis we can conclude that the loss of radar coherence in this study area is a function of both topographic and vegetation factors. This can be further verified by comparing the coherence values along the three profiles, AA′, BB′ and CC′ (see Fig. 3), with different topography and NDVI. The graphical and tabular comparisons are shown in Fig. 7 and Table 3, respectively. The relatively high coherence values ($M = 0.35$, SD = ±0.12) appear along the line CC′ with gentle topography and less vegetation, while the low coherence values appear along the line BB′ and CC′ with sig-

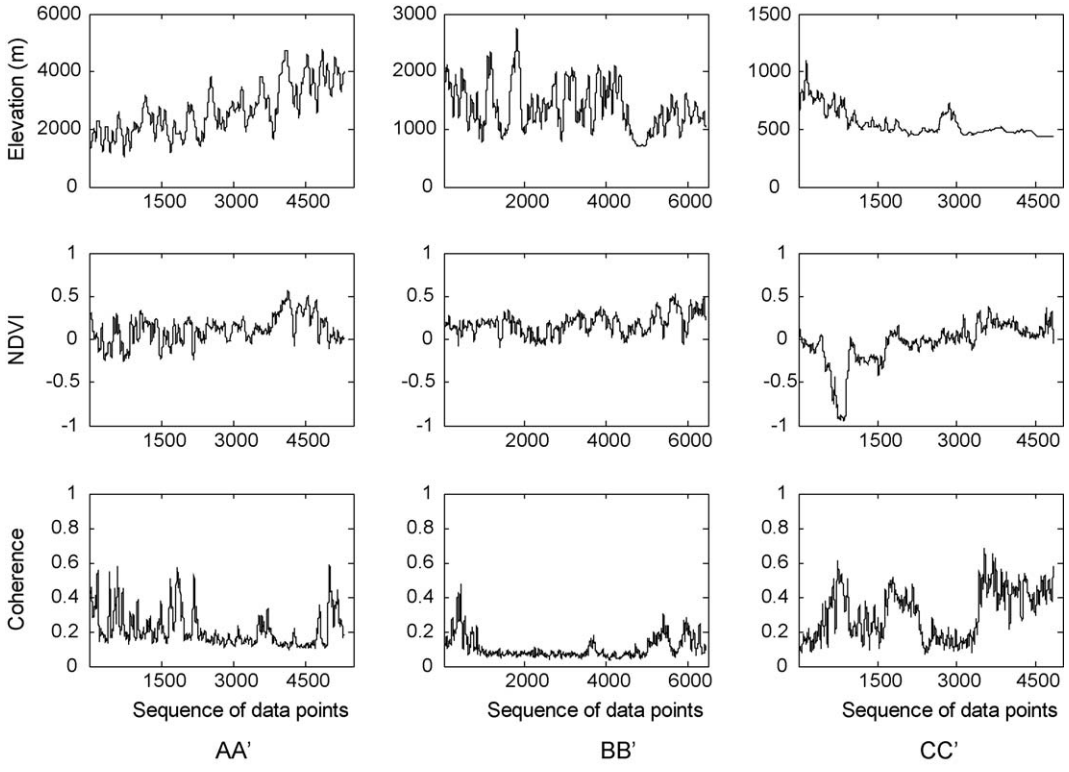

Fig. 7. The profiles of elevations, NDVI and coherence along line AA′, BB′ and CC′ (see Fig. 3).

Table 3
Comparison of coherence values along three profiles.

No.	Profile	Elevation (m)		NDVI		Coherence	
		M[a]	SD[a]	*M*	SD	*M*	SD
1	AA′	2643	±878	0.12	±0.16	0.21	±0.10
2	BB′	1375	±406	0.18	±0.12	0.10	±0.06
3	CC′	549	±118	−0.05	±0.24	0.35	±0.12

[a] *M* and SD denote mean and standard deviation, respectively.

nificant topography and dense vegetation. The coseismic ruptures are the main cause for the low coherence measurements of the line BB′.

As a final remark, the topographic factor tends to have a larger influence to radar coherence than the vegetation factor does. This can be exemplified by two areas, A and B, marked by ellipses in the same SAR coverage of path 474 (Fig. 5). Although the NDVI values in the two areas are similar, the coherence values in the area B with moderate topography are much higher than those in the area A with significant topography.

6. Summary and conclusions

The 2008 Ms8.0 Wenchuan earthquake occurred on the northeastern-striking thrust LMS faults beneath the rugged margin between the Qinghai-Tibet Plateau and Sichuan Basin. The mosaicked differential interferogram was generated using the 46 ALOS L-band SAR images to measure the surface deformation associated with the Wenchuan earthquake. The coseismic interferogram derived exhibits the remarkable fringes that reflect the significant surface displacements caused by the main shock. The entire fringes extend northeast and surround the LMS faults. It confirms that the coseismic surface ruptures coincide with the YX–BC and GX–AX faults, extending about 280 km from southwest of the Town of Yinxiu to north of Qingchuan County. The deformation gradients close to the faults are so large that the near-field displacements are not detectable in width of 6 km (toward Qingchuan) to 28 km (toward Yingxiu).

The surface displacements can be estimated and interpreted with the coseismic interferogram. The lands in the Sichuan Basin had moved 0.1–1.3 m toward the satellite along the radar LOS direction with an azimuth of 349.8° and an elevation angle of 51.3°, while the lands in the LMS area had moved 1.4 m at most away from the satellite. The near-field motions are apparently larger than the far-field ones. Such distribution of surface displacements can be explained by convergent movements of the thrust LMS faults.

By comparing with the GPS data at 16 sites, we have demonstrated that the centimeter-level accuracy ($M = 0.62$ cm, SD = ±1.97 cm) of deformation measurements can be achieved with the ALOS PALSAR interferometer. Due to the different principles in data collection and processing, the InSAR measurements at the near-field GPS sites are in disagreement with the GPS results (differing in 7–15 cm).

Although the study area is highly mountainous and heavily vegetated, the interferometric coherence of the L-band interferometer is acceptable for deformation extraction even over months to years. This highlights the obvious advantage of the long-wavelength SAR system in maintaining coherent radar backscattering due to its capability of penetrating plant canopies more deeply. The numerical analysis with NDVI and elevation data shows that the radar coherence level is governed largely by temporal and topographic factors. The coherence values in the areas with higher NDVI are smaller than those in the areas with lower NDVI. The coherence values in the farmlands of the flat Sichuan Basin are higher than those in the LMS areas with steep slopes. The topographic factor tends to have a larger influence to radar coherence than the vegetation factor.

Acknowledgements

This work was supported in part by the National Natural Science Foundation of China under Grant 40774004, the Program for New Century Excellent Talents in University under Grant NCET-08-0822, and the Scientific Research Foundation for the Returned Overseas Chinese Scholars. The authors would like to thank the Earth Remote Sensing Data Analysis Center (ERSDAC) for providing the ALOS PALSAR data and the U.S. Geological Survey for providing the SRTM DEM and Landsat imagery of the study area.

References

Burchfiel, B.C., Chen, Z., Liu, Y., Royden, L.H., 1995. Tectonics of the Longmen Shan and adjacent regions. International Geology Review 37 (8), 661–735.
Densmore, A.L., Ellis, M.A., Li, Y., Zhou, R., Hancock, G.S., Richardson, N., 2007. Active tectonics of the Beichuan and Pengguan faults at the eastern margin of the Tibetan Plateau. Tectonics 26 (TC4005), doi:10.1029/2006TC001987.
Ding, X.L., Liu, G.X., Li, Z.W., Li, Z.L., Chen, Y.Q., 2004. Ground subsidence monitoring in Hong Kong with satellite SAR interferometry. Photogrammetric Engineering & Remote Sensing 70 (10), 1151–1156.
Ding, X.L., Li, Z.W., Zhu, J.J., Feng, G.C., Long, J.P., 2008. Atmospheric effects on InSAR measurements and their mitigation. Sensors 8, 5426–5448.
Fukushima, Y., Ozawa, T., Hashimoto, M., 2008. Fault model of the 2007 Noto Hanto earthquake estimated from PALSAR radar interferometry and GPS data. Earth Planets Space 60, 99–104.
Ge, L.L., Zhang, K., Ng, A., Dong, Y., Chang, H.C., Rizos, C., 2008. Preliminary results of satellite radar differential interferometry for the co-seismic deformation of the 12 May 2008 Ms8.0 Wenchuan earthquake. Geographic Information Science 14 (1), 12–19.
Ghiglia, D.C., Pritt, M.D., 1998. Two-Dimensional Phase Unwrapping: Theory, Algorithms, and Software. John Wiley & Sons Ltd.
Hao, K.X., Si, H.J., Fujiwara, H., Ozawa, T., 2009. Coseismic surface-ruptures and crustal deformations of the 2008 Wenchuan earthquake Mw7.9, China. Geophysical Research Letters 36, L11303, doi:10.1029/2009GL037971.
Huang, R.Q., Li, W.L., 2009. Development and distribution of geohazards triggered by the 5.12 Wenchuan earthquake in China. Science in China (Series E) 52 (4), 810–819.
Lee, H., Liu, J.G., 2001. Analysis of topographic decorrelation in SAR interferometry using ratio coherence imagery. IEEE Transactions on Geoscience and Remote Sensing 39 (2), 223–232.
Li, Z., Fielding, E., Parsons, B., Wright, T., Feng, W., 2008. Fault trace and slip in the 2008 Mw 7.9 Sichuan, China earthquake from InSAR observations. Eos Transactions of AGU 89 (53) (Fall Meet. Suppl., Abstract G33C-0714).
Lin, A.M., Ren, Z.K., Jia, D., Wu, X.J., 2009. Co-seismic thrusting rupture and slip distribution produced by the 2008 Mw 7.9 Wenchuan earthquake, China. Tectonophysics 471, 203–215.
Liu, G.X., Ding, X.L., Li, Z.L., Li, Z.W., Chen, Y.Q., 2004. Pre- and co-seismic ground deformations of the 1999 Chi-Chi, Taiwan earthquake, measured with SAR interferometry. Computers & Geosciences 30 (4), 333–343.
Liu, G.X., 2006. Mapping of Ground Deformations with Radar Interferometry. Publishing House of Surveying and Mapping, Beijing.
Liu, G.X., Luo, X.J., Chen, Q., Huang, D.F., Ding, X.L., 2008. Detecting land subsidence in Shanghai by PS-networking SAR interferometry. Sensors 8, 4725–4741.
Liu, G.X., Buckley, S.M., Ding, X.L., Chen, Q., Luo, X.J., 2009. Estimating spatiotemporal ground deformation with improved persistent-scatterer radar interferometry. IEEE Transactions on Geoscience and Remote Sensing 47 (9), 3209–3219.
Massonnet, D., Rossi, M., Carmona, C., Adragna, F., Peltzer, G., Feigl, K., Rabaute, T., 1993. The displacement field of the Landers earthquake mapped by radar interferometry. Nature 364, 138–142.
Massonnet, D., Feigl, K.L., 1998. Radar interferometry and its application to changes in the Earth's surface. Reviews of Geophysics 36 (4), 441–500.
Pritchard, M.E., Simons, M., 2002. A satellite geodetic survey of large-scale deformation of volcanic centres in the central Andes. Nature 418, 167–171.

Rosen, P.A., Hensley, S., Joughin, I.R., Li, F.K., Madsen, S.N., Rodriguez, E., Goldstein, R.M., 2000. Synthetic aperture radar interferometry. Proceedings of the IEEE 88 (3), 333–382.

Shan, X.J., Qu, C.Y., Song, X.G., Zhang, G.F., Liu, Y.H., Guo, L.M., Zhang, G.H., Li, W.D., 2009. Coseismic surface deformation caused by the Wenchuan Ms8.0 earthquake from InSAR data analysis. Chinese Journal of Geophysics 52 (2), 496–504.

Sun, J.B., Liang, F., Shen, Z.K., Xu, X.W., 2008. InSAR deformation observation and preliminary analysis of the Ms8 Wenchuan earthquake. Seismology and Geology 30 (3), 789–795.

Takada, Y., Kobayashi, T., Furuya, M., Murakami, M., 2009. Coseismic displacement due to the 2008 Iwate-Miyagi Nairiku earthquake detected by ALOS/PALSAR: preliminary results. Earth Planets Space 61, e9–e12.

Vancutsem, C., Pekel, J.-F., Evrard, C., Malaisse, F., Defourny, P., 2009. Mapping and characterizing the vegetation types of the Democratic Republic of Congo using SPOT vegetation time series. International Journal of Applied Earth Observation and Geoinformation 11 (1), 62–76.

Wang, Q., Qiao, X., Wang, M., You, X., Freymueller, J.T., 2008. GPS-derived coseismic deformation associated with the 12 May 2008 Wenchuan earthquake. Eos Transactions of AGU 89 (53) (Fall Meet. Suppl., Abstract G33C-0716).

Wikipedia, 2009. Last accessed on 1 June 2009, http://en.wikipedia.org/wiki/List_of_2008_Sichuan_earthquake_aftershocks.

Yarai, H., Tobita, M., Nishimura, T., Amagai, T., Suzuki, A., 2008. A fault model of the 2008 Wenchuan earthquake estimated from SAR measurements. Eos Transactions of AGU 89 (53) (Fall Meet. Suppl., Abstract G33C-0709).

Zebker, H.A., Villasenor, J., 1992. Decorrelation in interferometric radar echoes. IEEE Transactions on Geoscience and Remote Sensing 30 (5), 950–959.

Zebker, H.A., Rosen, P.A., Goldstein, R.M., Gabriel, A., Werner, C.L., 1994. On the derivation of coseismic displacement fields using differential radar interferometry: the Landers earthquake. Journal of Geophysical Research 99 (19), 617–634.

Zhang, P.Z., 2008. Co-seismic deformation field of 2008 Ms8.0 Wenchuan earthquake revealed by GPS data. Science in China (Series D) 38 (10), 1195–1206.

Zhang, L., Wu, J.C., Ge, L.L., Ding, X.L., Chen, Y.L., 2008. Determining fault slip distribution of the Chi-Chi Taiwan earthquake with GPS and InSAR data using triangular dislocation elements. Journal of Geodynamics 45 (4–5), 163–168.